IEPC-95-1

High Power Arcjet Experiments and Analysis

Thomas M. Gölz, Monika Auweter-Kurtz, Helmut L. Kurtz and P. Christian Sleziona

Institut für Raumfahrtsysteme
Universität Stuttgart
Pfaffenwaldring 31
70550 Stuttgart, FRG

Abstract

The numerical simulation of thermal arcjet thrusters has become a field of increased importance in the last five years. At Stuttgart University the high power arcjet called HIPARC-R has been developed, built and successfully tested. The test results showed specific impulse values of more than 2000 s which had never been reached before with a thermal arcjet thruster. The mass flow rate was 150 mg/s resulting in a thrust value of 3 N and a specific input power of 670 $MWkg^{-1}s^{-1}$. For a further increase of the performance of these devices the more detailed knowledge of the processes inside such a thruster is required and therfore the numerical simulation of these processes has been focussed.

As a first step in calculating the viscous, reacting high enthalpy flow with electric arc the flow of the cold propellant gas without electric arc has been performed. The finite volume Navier-Stokes code *NSFLEX* has been used. Pressure, density, velocity, and temperature data are given for this test case. Arc chamber pressure and thrust values are compared with experimental data. First solutions for the current density distribution and the chemical equilibrium composition are also given in the paper.

1 Introduction

Thermal arcjet thrusters have been developed at the Institut für Raumfahrtsysteme (Space Systems Institute) at Stuttgart University since 1988. Since that time the thruster family has grown year by year, with the various devices being operated with different propellants and at power levels ranging from 600 W up to 120 kW.

The high power arcjet thruster HIPARC-R represents the most powerful member of this family. Its maximum attainable power level of more than 100 kW with at the same time excellent propellant throttling capabilities allow the realization of a very good specific impulse values of more than 2000 s.

The numerical simulation of magnetoplasmadynamic (MPD) thrusters and MPD plasma generators for plasma wind tunnel applications has been another field of interest at this institute. The viscous reacting arc flow has required the development of additional modules for available Navier-Stokes codes, such as a chemistry module, a module for the calculation of the electron temperature and the calculation of the transport coefficients in the plasma regime. With the numerical results for the MPD thruster on the one hand and the arcjet thruster on the other hand the idea arose to perform a numerical analysis of this arcjet thruster family; firstly to predict thruster performance in a regime that was not yet tested, to simulate risky operation points rather than run the experiments, and secondly to validate the numerical code with the experimental data taken from the thruster. The main intention of this research is the investigation of loss mechanisms and thus the further improvement of these thrusters.

As first steps in the computational analysis of the whole thruster system calculations of the cold gas flow with a chemical equilibrium composition will be presented. The Navier-Stokes code used is the *NSFLEX* of DASA-MBB, Munich, which has been adapted to internal flows by different IRS authors [11]. The thrusters are discretized with a curvilinear cylindrical grid. The boundary points are set by means of an IRS own code which offers the possibility to vary the spacing between the boundary points. The grid generation code *GRAPE* is used inside the flowfield in order to control grid spacing in the boundary layer.

2 Experimental Setup

2.1 Thruster

HIPARC-R is a constrictor type thermal arcjet with a conical nozzle at a half angle of 20°. The nozzle throat diameter is 4 mm, the constrictor length to diameter ratio is 1, the area ratio is 1:225. The converging part of the nozzle offers a 50° opening half angle. The cathode of 10 mm in diameter is mounted on the gas supply tube in the thruster's centerline. This diameter proved to be the best suited for this power level with the water cooled device [6]. The cathode tip is conical with a half angle of 30°. The most striking feature of HIPARC-R is the big nozzle corpus, which is fixed to the thruster housing by six pairs of TZM brackets (Fig. 1). These brackets ensure that the necessary force is exerted on the graphite sealing between nozzle body and thruster housing. This solution was selected because of cost and mass saving reasons. The nozzle dimensioning of HIPARC-R was based on thermal efficiency measurement data (obtained with the water cooled HIPARC [6, 5], data obtained with the 10 kW class thermal arcjet thrusters TT1 [4] and MARC [3], and data published by Sankovic and Curran [10]. A total of about 10% of the input power was expected to be radiated away from the thruster at an emissivity of 0.4. A maximum nozzle temperature of 2300 K led to an outer nozzle diameter of 70 mm at a length of 72 mm. The thruster sealing is done by graphite foil rings of 0.35 mm thickness. The sealing pressure force is supplied by the TZM brackets between nozzle and housing, by steel disks on the back side and by a spring made of Haynes alloy 230 inside the thruster. The propellant gas is fed by a stainless steel pipe at the thruster center. It is used as current supply and as cathode fixation. The gas is hereby used as the current supply cooling medium. It exits the pipe near the spring and is led to a channel between the thruster housing and main insulator, where it is heated regeneratively. It is injected into the arc chamber through four bore holes (of 0.75 mm in diameter each), directing axially to the cathode tip. A swirl is not induced.

HIPARC-R gives the possibility to measure the arc chamber pressure during thruster operation. A TZM pipe is screwed to the thruster housing, leading to a pressure tap (Fig. 2). The pipe is water cooled by a cooling sleeve at a distance of 30 cm off the thruster. It was intended to keep the temperature gradient and thus the heat conduction along the pipe as small as possible in order not to disturb the temperature distribution in the thruster. Cathode and anode are electrically insulated by parts made of boron nitride and a glass ceramics material (Macor), respectively. The cathode gap can be adjusted by a mechanism that allows adjustment before sealing the cathode pipe fed through. This adjustment device is covered by a steatite cap in order to prevent arc-overs to the thruster parts on anode potential.

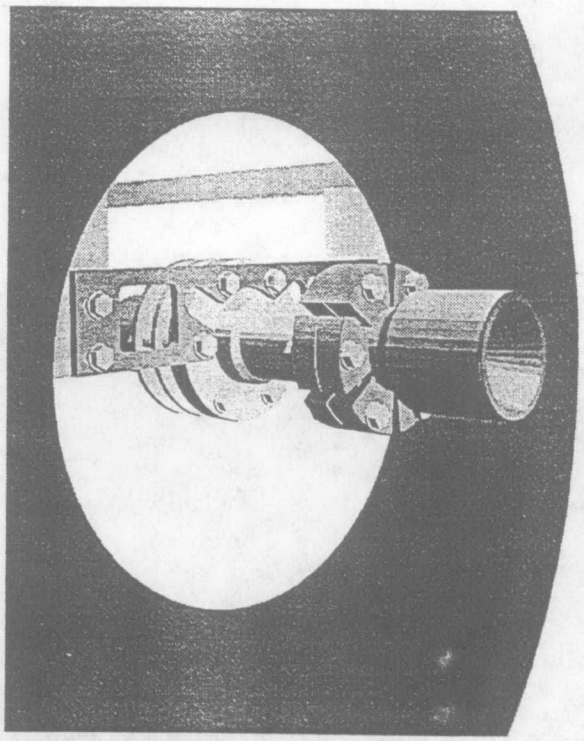

Fig. 1: HIPARC-R mounted onto the thrust balance

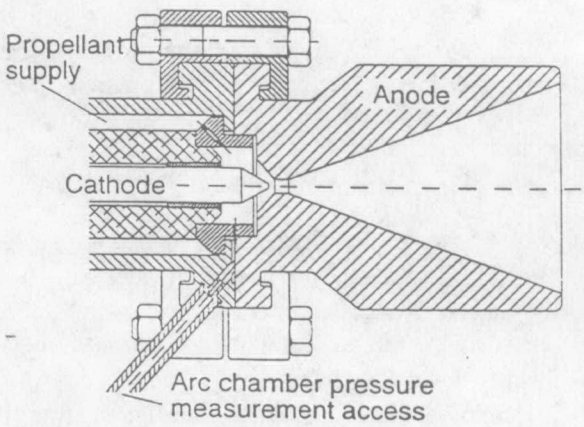

Fig. 2: HIPARC-R nozzle section with arc chamber pressure measurement access

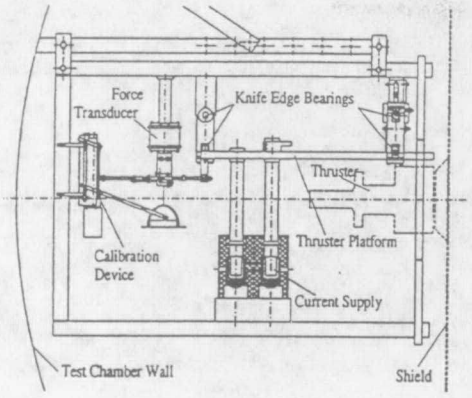

Fig. 3: The HIPARC thrust balance, used for HIPARC-R as well

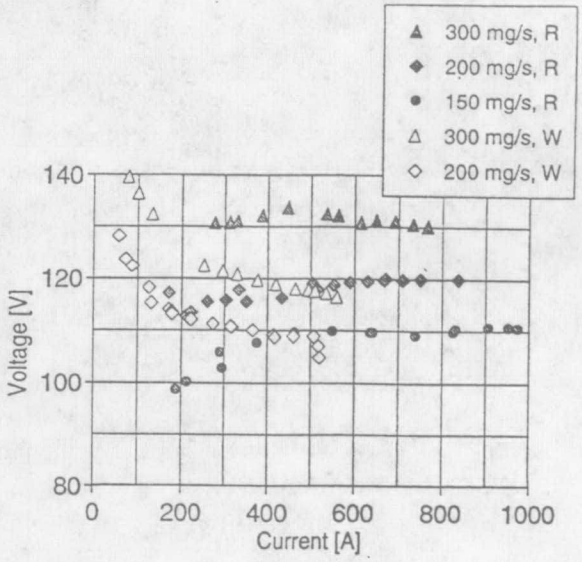

Fig. 4: Current/Voltage diagram (R: radiation cooled, W: water cooled)

2.2 Thrust Balance

The HIPARC-R thruster is mounted on the same thrust balance that was used for its watercooled predecessor HIPARC, which is an improved version of the IRS standard type (Fig. 3). The movable part of the balance carrying the thruster is suspended on three swing arms. Each swing arm is supported by two knife edge bearings. The thrust force is transmitted as a tension force by a thin wire over a reversing sheave to a water cooled measuring box that contains the force transducer. In order to allow the calibration of the balance under vacuum conditions, a remotely operated weight lever has been installed. This lever places a weight on a scale which creates a defined force on the platform.

The electric power is fed to the thruster via two copper rods submerged into mercury filled tubes. To avoid evaporation of the mercury, its surface is sealed by silicon oil.

The cooling water for the thruster/thrust balance interface and for the thrust balance structure will be fed to the platform by semicircular hoses allowing minimum stiffness. Effects of stiffness and friction are calibrated for each measuring sequence before ignition and checked after engine shut down under vacuum conditions.

2.3 Test Facilities

The HIPARC-R thruster and the thrust balance are integrated in a stainless steel tank of 4.5 m length and 2 m in diameter. This vacuum chamber is double-walled in order to provide water cooling of the tank during thruster operation. The vacuum system, the high current supply and the data acquisition system have been described in formerly published reports [4]. Three mass flow controllers calibrated for hydrogen have been integrated into the IRS gas supply system, enabling a wide range of propellant gas flows to be tested. The mass flow controller readout is checked by weight-balancing of the gas bottles with an accuracy of ± 1 g.

3 Performance Data

3.1 Electrical Magnitudes

The current/voltage characteristics of HIPARC-R look flatter than the one obtained with the water cooled counterpart; the voltage level is higher (Fig. 4).

The voltage increases with increasing current. This behaviour is typical for MPD devices or arcjet devices at high specific input power. It is to be noted that these data marked with "W" have been obtained with a nozzle throat diameter of 4 mm, where the 100 kW level could be reached only with a mass flow rate of 400 mg/s and where no comparable experiments have been performed yet with HIPARC-R.

3.2 Thrust Characterictics

The maximum mass flow rate currently tested with HIPARC-R was 300 mg/s H_2. At a maximum input power of 100 kW a thrust of 4.0 N was mea-

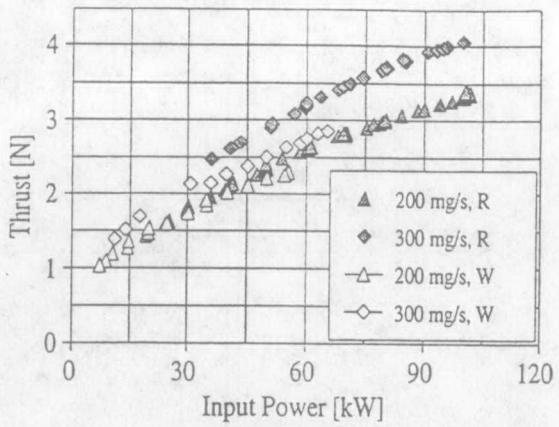

Fig. 5: Thrust versus input power for the radiation cooled (R) and the water cooled (W) thruster

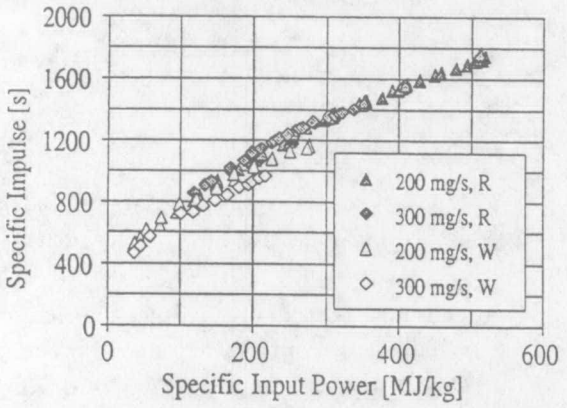

Fig. 6: Specific impulse versus specific input power for the radiation cooled (R) and the water cooled (W) thruster

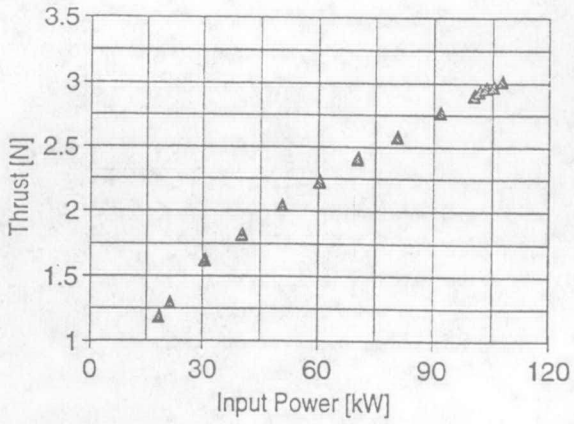

Fig. 7: Thrust versus input power at 150 mg/s

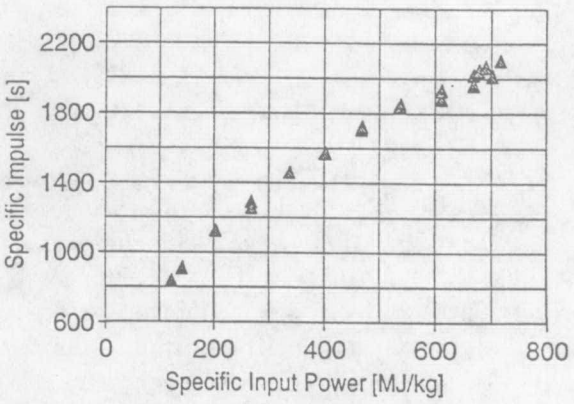

Fig. 8: Specific impulse versus specific input power at 150 mg/s

sured (Fig. 5). This leads to a specific impulse of almost 1400 s at a specific input power of 338 MW kg^{-1} s^{-1}. Better performance is reached with lower mass flow rates. At 200 mg/s a specific impulse of almost 1800 s could be achieved at 500 MJ/kg specific input power which equals an absolute input power of 100 kW.

The best results in terms of efficiency have been obtained with a mass flow rate of 200 mg/s. The thrust efficiency values range from 25 to 30%, depending on specific input power.

Encouraged by the thruster performance at high power operation, the mass flow rate was throttled down to 150 mg/s in order to increase the specific input power. Here the thruster could be operated in a stable mode as well, with the specific impulse increasing to 2000 s at 700 MJ/kg specific input power. A further increase of the input power was stopped by a failure of the current supply system during an increase of the current. The last current readout was 973 A yielding an input power of 107 kW. The current was limited to 1000 A in this experiment. Fig. 8 shows the specific impulse versus the specific input power for the 150 mg/s mass flow rate. Absolute values are given in Fig. 7, efficiency data is depicted in Fig. 9.

3.3 Arc Chamber Pressure

At a given power setting the arc chamber pressure is higher with the radiation cooled device than with the water cooled thruster [7]. This indicates a higher average temperature and thus a higher propellant gas enthalpy in the arc chamber. At the same time the thrust versus arc chamber pressure characteristic shows (almost) straight lines with different slopes for the water cooled and for the radiation cooled thruster version (Fig. 10). The steeper slope yields higher thrust values with the water cooled device

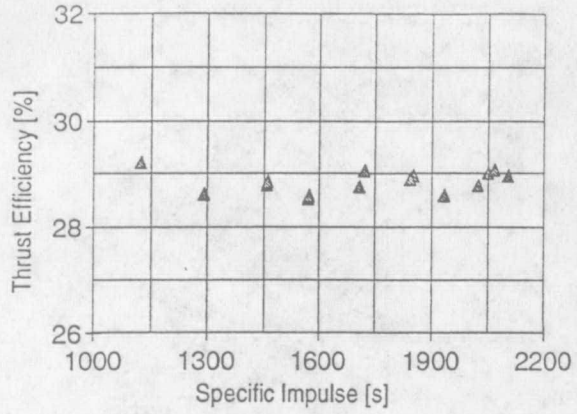

Fig. 9: Thrust efficiency versus specific impulse at 150 mg/s

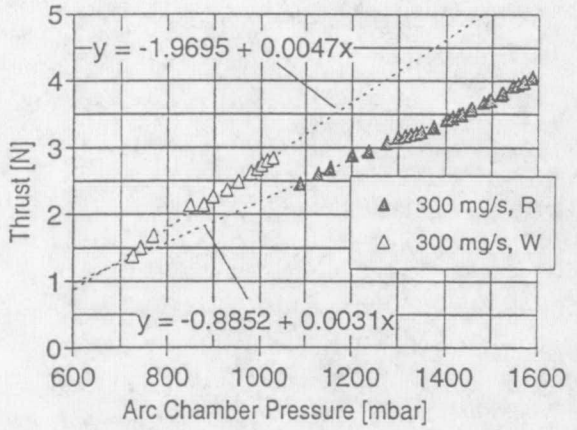

Fig. 10: Thrust versus arc chamber pressure. Comparison between water cooled and radiation cooled thruster

at the same value of the arc chamber pressure than with the radiation cooled device [8]. The equations representing the regression lines are also given in Fig. 10. As measurement of the arc chamber pressure was not possible in all test runs bacause the adaptor pipe to the pressure tap got broken during dismounting of the thruster, the feed line pressure was taken as an indicator for the arc chamber pressure instead. Fig. 10 shows the correlation of both pressure values with and without the arc burning.

4 Flow Field Characterization

4.1 Idealization

In reality the arcjet flow field represents a three dimensional viscous reacting turbulent gas flow in a transsonic velocity regime with high enthalpy and current discharge in the gas.

The idealized flow field is an axisymmetric laminar viscous reacting gas flow with an electric arc. The effects of current discharge and chemical reactions are taken into account by energy source terms due to ohmic heating and heat of reaction. For the calculation, the chemistry module, the current discharge code and the flow field code were combined to determine flow field, chemical composition and current density in the gas. These codes are coupled in the following manner: for a given flow field, the chemical composition is determined. With these results, the current density and after that again the flow field equations were integrated.

4.2 Flow Field Discretization

The flow field of the arcjet thruster is basically a channel flow with extremely varying cross sections. In the converging part of the nozzle the channel cross section decreases by a factor of 10, where it increases by a factor of 225 in the diverging part of the nozzle. The Figures 2 and 11 show the parts of the physical flow field. The space between the thruster and the tank walls is filled with gas at the ambient tank pressure of several Pascal.

For the calculation an idealized flow field is used. It covers the arc chamber, the nozzle and a half sphere in the outflow region in order to incorporate the appropriate outflow boundary conditions. Because of difficulties with creating a grid of the full arc chamber, constrictor, nozzle and outflow section, the arc chamber with the gas injectors is omitted in the grid and is replaced by a line with a parabolic velocity profile. In order to save memory and CPU time and because of the axisymmetry only the part between the symmetry line and the thruster walls is calculated.

Figure 12 shows the constrictor section of the grid. The constrictor has a diameter and a length of 4 mm. Figure 13 shows the outer edge of the nozzle, around which the grid is constructed in order to model the flow separation from the nozzle correctly.

4.3 Flow Field Solver

For the description of the two-dimensional, axisymmetric, viscous flow the following form of the Navier-Stokes equations with curvilinear, cylindri-

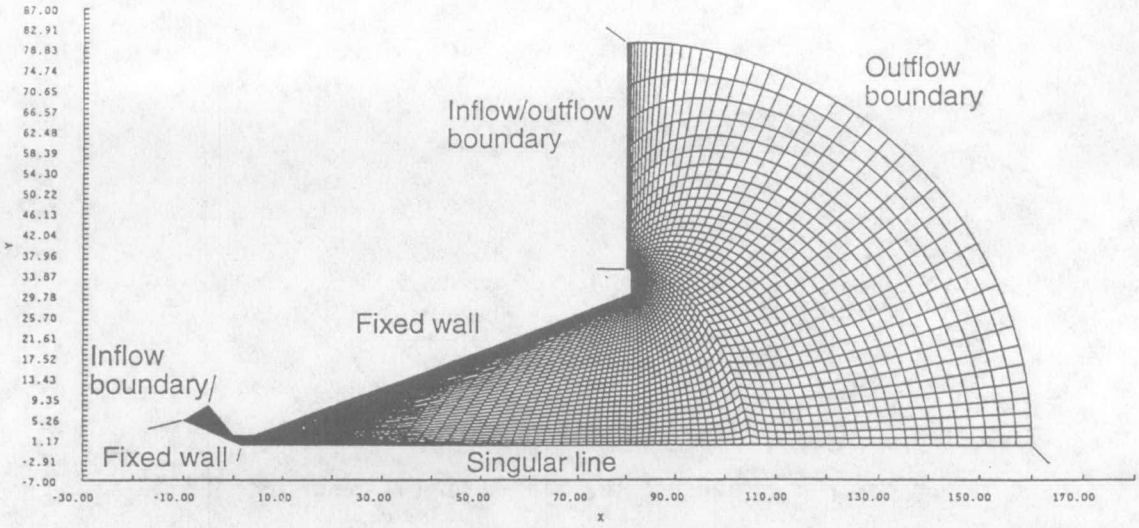

Fig. 11: Complete computational grid of HIPARC-R

cal coordinates have been used:

$$\frac{\partial}{\partial t}\mathbf{q}+\frac{\partial}{\partial \xi}\mathbf{E}(\mathbf{q})+\frac{\partial}{\partial \eta}\mathbf{F}(\mathbf{q})+\mathbf{H}(\mathbf{q})=\frac{1}{\mathrm{Re}}\left(\frac{\partial}{\partial \xi}\mathbf{P}+\frac{\partial}{\partial \eta}\mathbf{S}\right). \tag{4.1}$$

The indices t,ξ,η indicate the partial differentiation with respect to time and to the ξ- and η-direction. The vector of variables $\mathbf{q}$ and the vector $\mathbf{H}(\mathbf{q})$ are

$$\mathbf{q}=\begin{bmatrix}\rho\\ \rho u\\ \rho v\\ e\end{bmatrix}, \tag{4.2}$$

$$\mathbf{H}(\mathbf{q})=\frac{1}{J}\begin{bmatrix}\rho v/r\\ \rho uv/r\\ \rho v^2/r\\ (p+e)v/r-\varepsilon_{diss}\mathrm{d}n_N/\mathrm{d}t|_{react}\end{bmatrix}. \tag{4.3}$$

The ξ-flux vector $\mathbf{E}(\mathbf{q})$ is

$$\mathbf{E}(\mathbf{q})=\frac{1}{J}\begin{bmatrix}\rho U\\ \rho uU+\xi_z p\\ \rho vU+\xi_r p\\ (e+p)U-\xi_t p\end{bmatrix}. \tag{4.4}$$

The η-flux vector as well as the viscous flux vectors $\mathbf{P}$ and $\mathbf{Q}$ are analogous. U is the contravariant velocity, r and z are the cylindrical coordinates, t is the time, and ξ, η are the curvilinear coordinates. ξ_z stands for the derivative of ξ with respect to z. u, v are the Cartesian velocities whereas ρ is the total mass density and e is the total energy. The Jacobian J is

$$J=\left(z_\xi r_\eta - z_\eta r_\xi\right)^{-1}. \tag{4.5}$$

The total pressure is obtained by using

$$p=(\gamma-1)\left[e-\frac{1}{2}\rho\left(u^2+v^2\right)\right]. \tag{4.6}$$

Herein γ is the adiabatic coefficient.

The finite volume code *NSFLEX* of DASA-MBB which is used here for the solution is a finite volume code using MUSCL type flux difference splitting. The implicit equations are solved using a Gauss-Seidel relaxation technique.

4.4 Boundary Conditions

The flow field boundary lines are grouped in five different classes:

1. At fixed walls the no slip condition for viscous flow has to be satisfied, so the velocity is set to zero at the fixed wall.

2. At the symmetry line a "singular line" boundary condition is used. The radial component of the velocity is zero, whereas the axial component, density and total energy are set to a value so that the lines of constant value intersect the singular line normal to the axis.

3. The gas inflow is discretized as a so-called supersonic inflow, i.e. the inflow velocity vector perpendicular to the boundary line is set to a value so that the mass flow rate resulting from the total pressure and the Mach number in the inflow boundary is equal to the value set in the experiment.

4. At the outflow boundary the total pressure is set to 10 Pa, which is the value measured in the experiment. The velocities are extrapolated from next upstream cells.

5. The part of the boundary that limits the space between the outflow half sphere and the thruster nozzle, which represents a vertical disk, has the so-called subsonic inflow/outflow boundary condition. At this boundary it is not clear beforehand in which direction the gas flows. Here the total pressure and temperature values are set according to experimental data.

4.5 Solution of the Current Discharge Equation

The calculation of the current distribution supplies the current density at all field points. The current density determines one part of the overall heat source term. The determining equations are Maxwell's equations

$$\nabla \times \vec{B} = \mu_0 \vec{j} \qquad (4.7)$$

$$\nabla \times \vec{E} = 0 \qquad (4.8)$$

$$\nabla \cdot \vec{B} = 0 \qquad (4.9)$$

$$\nabla \cdot \vec{E} = 0 \qquad (4.10)$$

and Ohm's law for plasma

$$\vec{j}=\sigma\left(\vec{E}+\vec{v}\times\vec{B}\right)-\frac{\omega\tau}{B}\left(\vec{j}\times\vec{B}-\nabla p_e\right). \qquad (4.11)$$

Introducing the hall parameter β as $\omega_e\tau_e/(B\sigma)$, where ω_e is the electron cyclotron frequency, τ_e is the inverse collision frequency, B is the magnetic induction and σ is the electrical conductivity of the plasma.

This leads to

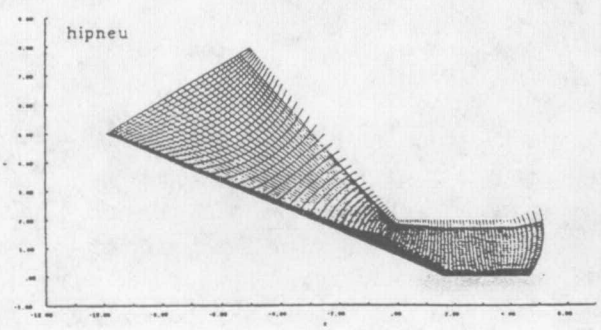

Fig. 12: Computational grid: constrictor section

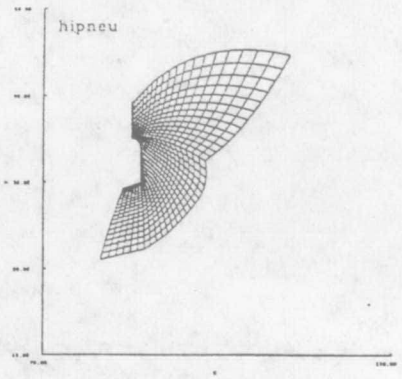

Fig. 13: Computational grid: nozzle edge section

$$\vec{E}=\frac{\vec{j}}{\sigma}-\vec{v}\times\vec{B}+\beta\left(\vec{j}\times\vec{B}-\nabla p_e\right). \qquad (4.12)$$

With the definition of the electric potential function $\Psi=rB_\varphi$ and after the evaluation of the nabla-expressions in (4.12) using (4.8) the following equation is obtained:

$$\begin{aligned} 0 = {} & \frac{\partial^2\Psi}{\partial z^2}+\frac{\partial^2\Psi}{\partial r^2} \\ & -\frac{\partial\Psi}{\partial r}\left(\frac{1}{r}+\frac{1}{\sigma}\frac{\partial\sigma}{\partial r}\right. \\ & \qquad \left.-\sigma\frac{\Psi}{r}\frac{\partial\beta}{\partial z}+\sigma\mu_0 u\right) \\ & -\frac{\partial\Psi}{\partial z}\left(\frac{1}{\sigma}\frac{\partial\sigma}{\partial z}-2\sigma\beta\frac{\Psi}{r^2}\right. \\ & \qquad \left.+\sigma\frac{\Psi}{r}\frac{\partial\beta}{\partial r}+\mu_0\sigma w\right) \\ & -\sigma\mu_0\Psi\left(\frac{\partial w}{\partial z}+\frac{\partial u}{\partial r}-\frac{u}{r}\right) \\ & +\sigma\mu_0 r\left(\frac{\partial\beta}{\partial z}\frac{\partial p_e}{\partial r}-\frac{\partial p_e}{\partial z}\frac{\partial\beta}{\partial r}\right). \end{aligned} \qquad (4.13)$$

This equation was solved by a finite difference scheme using a SLOR-method (successive line over-relatation).

The boundary conditions have been taken from measurements of the current distribution with the water cooled HIPARC-thruster [6]. The discrete segment current portion values have been transformed to a steady current density function taking into account that the surface area of the anode segmnets increases towards the nozzle exit.

Measurements of the anode surface temperature distribution indicate that the area of maximum heat load is close to the constrictor, so that the assumption

of the two current distributions being similar seems to be justified.

For the current density calculation starting from the cold gas flow a uniform electrical conductivity is supposed in order to establish current flow. This value remains the minimum conductivity in the further calculation.

4.6 Electron Energy Equation

The electron temperature has a strong effect on the electrical and thermal conductivity and on the electron density, which again influences the discharge pattern. Therefore, a two-dimensional code for the electron temperature distribution, corresponding to the two-dimensional discharge code, was written. The electron temperature distribution is determined by the thermal energy equation for the electron component of the plasma.

$$\nabla(\lambda_e \nabla T_e) + \frac{5}{2}\frac{k}{e}\vec{j}\nabla T_e + p_e \nabla \cdot \vec{v} = \frac{\vec{j}^2}{\sigma} - \sum_{\nu} n_\nu n_e \alpha_{e\nu}(T_e - T_h) - W_i \left.\frac{\partial n_e}{\partial t}\right|_{rct} \quad (4.14)$$

The subscript ν represents the heavy particles. The first term on the left hand side represents the conductive heat flux in the electron gas, and the second term gives the convective heat flux of the electron gas due to the electron drift. The energy input due to ohmic heating is represented by the first term on the right hand side. The sum of losses due to the energy transfer from the electron gas to the heavy particles gas is calculated by the second term on the right hand side. The reaction losses are given by the last term, where W_i is given by Unsöld.[13] The heat transfer coefficient $\alpha_{e\nu}$ and the thermal conductivity λ_e depend on the electron temperature,[9] where the heat transfer coefficient is

$$\alpha_{e\nu} = \frac{8\sqrt{2}}{\sqrt{\pi}} Q_{e\nu} \sqrt{\mu_{e\nu} k T_{e\nu}} \frac{k}{m_e + m_\nu} \quad (4.15)$$

and the thermal conductivity:

$$\lambda_e = \frac{15}{8}\sqrt{\frac{\pi}{2}} \frac{n_e k^2 T_e}{\sum_{\nu(=e)} n_\nu Q_{e\nu} \sqrt{m_{e\nu} k T_{e\nu}}} \quad (4.16)$$

In the sum of this conductivity equation ν also includes the electron component. For ν=e the collision cross section Q_{ee} can be set equal to the Gvosdover cross section.[2]

With respect to the rotational symmetry, equation 4.14 results in the following elliptical, partial differential equation of 2nd order:

$$\begin{aligned} &\lambda_e T_e^{\frac{5}{2}} \frac{\partial^2 T_e}{\partial r^2} + \lambda_e T_e^{\frac{5}{2}} \frac{\partial^2 T_e}{\partial z^2} \\ &+ \frac{5}{2}\lambda_e T_e^{\frac{3}{2}} \left(\frac{\partial T_e}{\partial r}\right)^2 + \frac{5}{2}\frac{k}{e}\frac{\partial T_e}{\partial r} j_r + \frac{5}{2}\frac{k}{e} T_e \frac{\partial j_r}{\partial r} \\ &+ \frac{5}{2}\lambda_e T_e^{\frac{3}{2}} \left(\frac{\partial T_e}{\partial z}\right)^2 + \frac{5}{2}\frac{k}{e}\frac{\partial T_e}{\partial z} j_z + \frac{5}{2}\frac{k}{e} T_e \frac{\partial j_z}{\partial z} \\ &+ \frac{\lambda_e T_e^{\frac{5}{2}}}{r}\frac{\partial T_e}{\partial r} + \frac{5}{2}\frac{k}{e}\frac{1}{r} T_e j_r + n_e k T_e \left(\frac{1}{r}\frac{\partial (rv)}{\partial r} + \frac{\partial u}{\partial z}\right) \\ &+ \frac{\vec{j}^2}{\sigma} - n_\nu n_e \alpha_{e\nu}(T_e - T_h) - W_i \left.\frac{\partial n_e}{\partial t}\right|_{rct} = 0 \end{aligned} \quad (4.17)$$

Here j_r and j_z are the current densities in the cylindrical $r-$ and $z-$directions.

4.7 Chemical Reactions

Due to the ohmic heating of the propellant and the subsequent expansion in the nozzle the hydrogen gas undergoes the following reactions:

$$H^+ + e + M \Rightarrow H + M \quad (4.18)$$
$$H + M \Rightarrow H^+ + e + M \quad (4.19)$$
$$H^+ + e + e \Rightarrow H + e \quad (4.20)$$
$$H + e \Rightarrow H^+ + e + e \quad (4.21)$$
$$H^+ + e \Rightarrow H + h\nu \quad (4.22)$$
$$H + H + M \Rightarrow H_2 + M \quad (4.23)$$
$$H_2 + M \Rightarrow H + H + M \quad (4.24)$$
$$H_2 + e \Rightarrow H + H + e \quad (4.25)$$

In the current program version this reaction scheme is solved under the assumption of local thermodynamical equilibrium (LTE) conditions, i.e. the reaction rates are fast enough to ensure chemical equilibrium at each field point. The solution was obtained using Frie's method [1].

5 Results

The obtained results of the cold gas flow calculation show a flow developing to an almost parallel nozzle (Figure 14) flow with an axial velocity profile as it is shown in Figure 16. The maximum velocity is located on the centerline, the boundary layer has a thickness of almost a third of the nozzle exit radius. The velocity vectors of this boundary layer region

is depicted in Figure 15. It can be seen that a flow separation does not occur, obviously because of the low pressure at the outflow boundary. Plots of lines of constant velocity are shown in Figure 17 (Axial velocity) and in Figure 18 (Radial velocity).

The translational temperature decreases to a value of 60 K in the expansion. The maximum of 422 K which is found at the joint point of outflow boundary and inflow/outflow boundary is probably due to incompatibilities of the different boundary conditions. Physically the temperature cannot supersede the inflow total temperature of 300 K.

In order to validate the results, the thrust resulting from the numerical data was compared with the cold gas thrust data obtained in the experiment. At a mass flow rate of 100 mg/s, which is the case calculated, a cold gas thrust of 0.24 N has been measured. In the calculation the thrust was determined by integrating over the cells at a specific ξ-coordinate, where each thrust element was calculated as

$$\Delta F = \Delta A_{\perp}\, \Delta \dot{m}\, u \qquad (5.26)$$

with $\Delta A_{\perp}$ being the projection of the cell exit plane area to a plane perpendicular to the thruster axis, $\Delta \dot{m}$ being the mass flow rate through this area and u being the axial component of the velocity vector.

The mass conservation is also checked this way. The total mass flow rate at each control area is determined by summation of the mass flow rates in each cell

$$\Delta m = \rho\, \Delta A\, (\vec{n} \cdot \vec{q})\,. \qquad (5.27)$$

with $\vec{n}$ being the normal vector of the cell exit area and $\vec{q}$ being the velocity vector. Figure 20 shows the mass flow rate at different areas ξ=const.. The abscissa indicates the ξ-coordinate, where ξ=132 represents the nozzle exit plane.

The plot shows a good conservation of the mass flow inside the thruster. Downstream the nozzle exit this check is not applicable because a certain amount of gas exits the control volume via the "inflow/outflow boundary", cf. Figure 11. This does not account for the mass flow through ξ=const. areas. The thrust resulting from this calculation equals 0.252 N at the nozzle exit plane. This fits the measured value very well.

6 Conclusion

In the numerical simulation of the high power thermal arcjet thruster HIPARC-R results of the cold gas

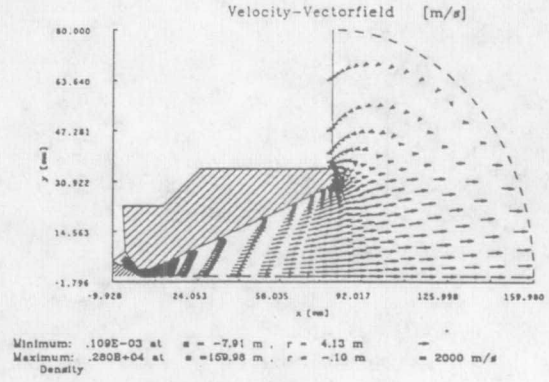

Fig. 14: Velocity vectorfield

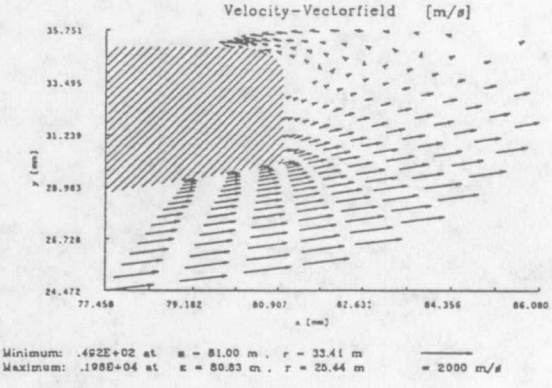

Fig. 15: Velocity vectorfield at the nozzle edge

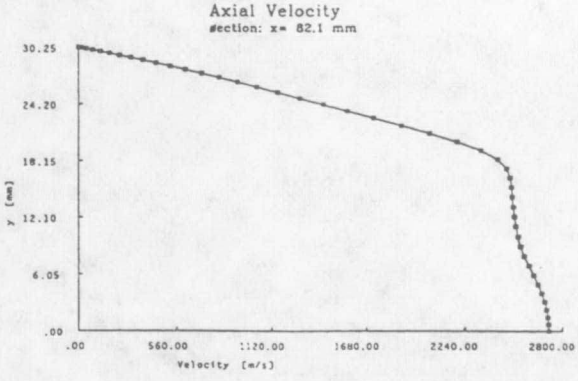

Fig. 16: Axial velocity profile at nozzle exit cross section

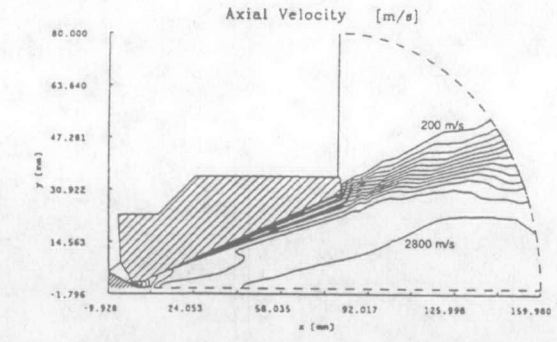

Fig. 17: Axial velocity plot

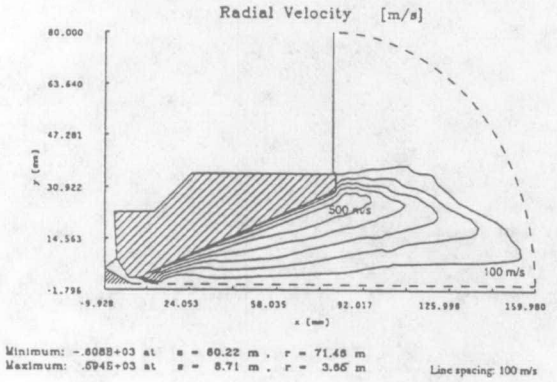

Fig. 18: Radial velocity plot

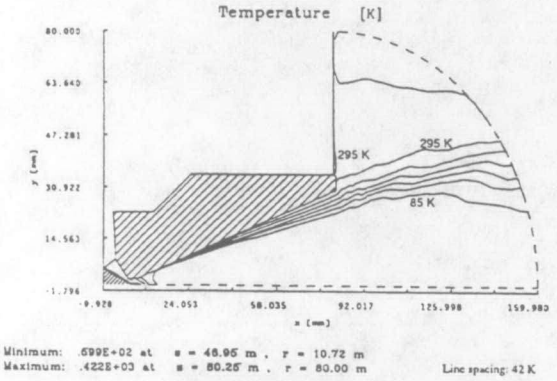

Fig. 19: Translational temperature plot

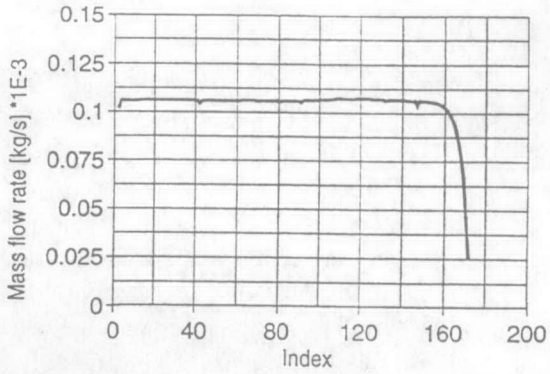

Fig. 20: Mass flow rate at coordinate lines ξ=const;$\dot{m}$=100 mg/s

calculation have been presented. The results of the calculation fit the measurement data very well. It showed that the calculation is very sensitive to the inflow boundary conditions, especially the setting of the pressure in the inflow boundary. The implementation of another boundary condition for the inflow is planned.

As the next steps the solution of the discharge equations are planned, so that ohmic heating terms are incorporated.

7 Acknowledgement

This work was supported by the German Science Society (Deutsche Forschungsgemeinschaft, DFG). This support is greatly acknowledged.

References

[1] J. Artmann and W. L. Bohn, 'Berechnung der Plasmakomponenten in Wasserstoff und Helium', in *Deutsche Luft- und Raumfahrt, Forschungsbericht 65-10*. Deutsche Versuchsanstalt für Luft- und Raumfahrt (in German), (1965).

[2] Finkelnburg, W. und Maecker, H.: *Elektrische Bögen und thermisches Plasma*. Handbuch der Physik Bd. XXII, Gasentladungen II, Springer, Berlin 1956

[3] B. Glocker and M. Auweter-Kurtz, 'Numerical and experimental constrictor analysis of a 10 kw thermal arcjet', in *28th Joint Propulsion Conference, Nashville, TN*, number AIAA 92-3835, (1992).

[4] B. Glocker, M. Auweter-Kurtz, T. M. Gölz, H. L. Kurtz, and H. O. Schrade, 'Medium power arcjet thruster experiments', in *21st International Electric Propulsion Conference, Orlando, FL*, number AIAA 90-2531, (1990).

[5] T. Gölz, M. Auweter-Kurtz, and H. L. Kurtz, '100 kW hydrogen arcjet thruster experiments', in *28th Joint Propulsion Conference, Nashville, TN*, number AIAA 92-3836, (1992).

[6] T. Gölz, M. Auweter-Kurtz, H. L. Kurtz, and H. O. Schrade, 'High power arcjet thruster experiments', in *22nd International Electric Propulsion Conference, Viareggio, Italy*, number IEPC-91-072, (1991).

[7] T. M. Gölz, M. Auweter-Kurtz, and H. L. Kurtz, 'Development and testing of a 100 kW radiation cooled thermal hydrogen arcjet thruster', in *23rd International Electric Propulsion Conference, Seattle, WA*, number IEPC-93-221, (1993).

[8] H. L. Kurtz, M. Auweter-Kurtz, B. Glocker, W. Merke, and H. O. Schrade, 'A 15 kw experimental arcjet', in *20th International Electric Propulsion Conference, Garmisch-Partenkirchen, FRG*, number IEPC 88-107, (1988).

[9] Schrade, H.O., Sleziona, P.C.:*Basic Processes of Plasma Propulsion.* Interim Scientific Report, AFOSR Grant 86-0337, June 1990

[10] J. M. Sankovic and F. M. Curran, 'Arcjet thermal characteristics', in *27th Joint Propulsion Conference, Sacramento, CA*, number AIAA 91-2456, (1991).

[11] P. C. Sleziona, M. Auweter-Kurtz, and H. O. Schrade, 'Numerical calculation of a nozzle type and cylindrical mpd thrusters', in *28th Joint Propulsion Conference, Nashville, TN*, number AIAA 92-3296, (1992).

[12] P.C. Sleziona, M. Auweter-Kurtz, B. Glocker, T. H. Gogel, T. M. Gölz, E. W. Messerschmid, and H. O. Schrade, 'Nonequilibrium flow in an arc heated wind tunnel', in *Hypersonic Flows in Reentry Problems. Test Gases: Experiment and Computations*. Proceedings of the Workshop of Hypersonic Flow for Reentry Problems, Antibes, France, 1990, Springer Verlag, Berlin/New York, (1991).

[13] Unsöld, A.: *Physik der Sternatmosphären.* Springer, Berlin·Heidelberg·New York, 1968